An enhanced finite volume method to model 2D linear elastic structures

R. Suliman[a,b,*], O.F. Oxtoby[b], A.G. Malan[b], S. Kok[a,c]

[a] *Department of Mechanical and Aeronautical Engineering, University of Pretoria, Pretoria, 0002, South Africa*
[b] *Advanced Computational Methods, Aeronautics Systems, Council for Scientific and Industrial Research, Pretoria 0002, South Africa*
[c] *Advanced Mathematical Modelling, Modelling and Digital Science, Council for Scientific and Industrial Research, Pretoria 0002, South Africa*

Abstract

This paper details the evaluation and enhancement of the vertex-centred finite volume method for the purpose of modelling linear elastic structures undergoing bending. A matrix-free edge-based finite volume procedure is discussed and compared with the traditional isoparametric finite element method via application to a number of test-cases. It is demonstrated that the standard finite volume approach exhibits similar disadvantages to the linear Q4 finite element formulation when modelling bending. An enhanced finite volume approach is proposed to circumvent this and a rigorous error analysis conducted. It is demonstrated that the developed finite volume method is superior to both standard finite volume and Q4 finite element methods, and provides a practical alternative to the analysis of bending-dominated solid mechanics problems.

*Correspondence to: CSIR Advanced Computational Methods, Building 12, P.O. Box 395, Pretoria 0001, South Africa. Tel: +27 (0)12 841 4004, Fax: +27 (0)86 5494768
Email address: rsuliman@csir.co.za (R. Suliman)

Keywords: finite volume, finite element, locking, error analysis

1. Introduction

Since the 1960s, the finite element method has mainly been used for modelling the mechanics of solids [1]. The finite volume method [2] has traditionally been more dominant in the field of fluid mechanics but has become increasingly popular for use in solid mechanics. Both schemes can be considered as methods of weighted residuals where they differ in the choice of the weighting function. The finite element Galerkin method uses shape functions as the weighting functions, while the finite volume method results by choosing the weighting function as unity. Finite element methods are typically formulated in a total Lagrangian or undeformed configuration. In contrast, finite volume methods are traditionally based on an Eulerian or updated mesh configuration, which is not optimal for solid mechanics problems.

Many studies have been conducted over the last two decades on the application of the finite volume method to linear elastic structures [3, 4, 5, 6, 7, 8]. It has also been extended to incompressible material deformation analysis [9, 10] and problems involving material non-linearities [11, 12]. Finite volume methods incorporating rotational degrees of freedom in addition to the displacement degrees of freedom have been presented in [10, 13]. A comparison between the finite volume and finite element method for geometrically non-linear solid mechanics was done by Fallah et al. [14], in which they conclude that the accuracy of the finite volume method is comparable to the finite element method on similar meshes. On the other hand, Vaz Jr. et al. [15] state that the finite element formulation provides higher accuracy

for displacement solutions.

It is well known that the linear finite element formulation suffers from sensitivity to element aspect ratio or shear locking when subjected to bending [16]. Fallah [8] and Wheel [6] present a locking-free finite volume approximation to Mindlin-Reissner plates for both cell-centred and vertex-centred formulations. However, using solid elements, Wenke and Wheel [13] present results that do indicate shear locking with the displacement-based vertex-centred finite volume approach and show that this is overcome by introducing additional rotational degrees of freedom. In this paper we present a new displacement-based finite volume method and show that it does not suffer from locking.

At the commencement of this study, a stable and robust in-house fluid-flow solver based on the compact edge-based finite volume approach [17, 18], is available. This study was undertaken to investigate whether the same edge-based vertex-centred finite volume approach could be easily extended to accurately model the mechanics of solids. There are distinct advantages in applying an edge-based approach. It is applicable to arbitrary element shapes and is computationally efficient. It is also particularly well suited to distributed memory parallel hardware architectures.

The governing equations together with the constitutive relations are presented in the next section. A description of the standard vertex-centred finite volume discretisation procedure, as well as a new hybrid finite volume approach is given in Section 3. This is followed by a detailed description of the numerical solution procedure in Section 4. In Section 5, we apply the two finite volume approaches to a number of test-cases and compare the results

with those from the standard Galerkin finite element method. An in-depth error analysis of the finite volume methods is shown in Section 6 and finally some conclusions are made.

2. Governing Equations

Consider a homogeneous isotropic elastic solid. The governing equations for the solid undergoing linear elastic motion, in the absence of any body forces, may be written in strong form as follows:

$$\frac{\partial \sigma_{ij}}{\partial x_j} = \rho a_i, \tag{1}$$

where σ_{ij} is the stress tensor, ρ is the density and a_i is the acceleration.

2.1. Constitutive equations

In order to solve the elastic boundary value problem, Equation (1), a relationship between stress and displacement is required. This relation is obtained indirectly through the strain. Assuming a linear constitutive relation, the stress tensor, σ_{ij}, is related to the strain tensor, ε_{ij}, by

$$\sigma_{ij} = \mathcal{C}_{ijkl}\varepsilon_{ij}, \tag{2}$$

where $\mathcal{C}$ is the fourth order elasticity tensor. For convenience, we can represent the stress and strain tensors as vectors and the fourth order elasticity tensor as a matrix. Furthermore, assuming an isotropic, hyperelastic St-Venant-Kirchoff material model, Equation (2) can be rewritten as

$$\begin{Bmatrix} \sigma_{11} \\ \sigma_{22} \\ \sigma_{33} \\ \sigma_{12} \\ \sigma_{13} \\ \sigma_{23} \end{Bmatrix} = b \begin{bmatrix} 1 & \frac{\nu}{1-\nu} & \frac{\nu}{1-\nu} & 0 & 0 & 0 \\ \frac{\nu}{1-\nu} & 1 & \frac{\nu}{1-\nu} & 0 & 0 & 0 \\ \frac{\nu}{1-\nu} & \frac{\nu}{1-\nu} & 1 & 0 & 0 & 0 \\ 0 & 0 & 0 & \frac{1-2\nu}{2(1-\nu)} & 0 & 0 \\ 0 & 0 & 0 & 0 & \frac{1-2\nu}{2(1-\nu)} & 0 \\ 0 & 0 & 0 & 0 & 0 & \frac{1-2\nu}{2(1-\nu)} \end{bmatrix} \begin{Bmatrix} \varepsilon_{11} \\ \varepsilon_{22} \\ \varepsilon_{33} \\ \gamma_{12} \\ \gamma_{13} \\ \gamma_{23} \end{Bmatrix} \tag{3}$$

where b is a constant defined as

$$b = \frac{E(1-\nu)}{(1+\nu)(1-2\nu)} \tag{4}$$

and E is the Young's modulus and ν is the Poisson's ratio of the material.

Considering only two-dimensional cases, two possibilities exist to simplify the analysis. These are conditions of plane stress and plane strain. The plane stress condition exists when the body is very thin, i.e. in the limit where the third dimension approaches zero. Under such conditions Equation (3) simplifies to:

$$\begin{Bmatrix} \sigma_{11} \\ \sigma_{22} \\ \sigma_{12} \end{Bmatrix} = \frac{E}{(1-\nu^2)} \begin{bmatrix} 1 & \nu & 0 \\ \nu & 1 & 0 \\ 0 & 0 & \frac{1-\nu}{2} \end{bmatrix} \begin{Bmatrix} \varepsilon_{11} \\ \varepsilon_{22} \\ \gamma_{12} \end{Bmatrix}. \tag{5}$$

The plane strain condition exists when the body is very thick, i.e. in the limit where the third dimension approaches infinity. Equation (3) now becomes:

$$\begin{Bmatrix} \sigma_{11} \\ \sigma_{22} \\ \sigma_{12} \end{Bmatrix} = \frac{E(1+\nu)}{(1-2\nu)} \begin{bmatrix} 1-\nu & \nu & 0 \\ \nu & 1-\nu & 0 \\ 0 & 0 & \frac{1-2\nu}{2} \end{bmatrix} \begin{Bmatrix} \varepsilon_{11} \\ \varepsilon_{22} \\ \gamma_{12} \end{Bmatrix}. \tag{6}$$

Finally, to close the governing equations, the relationship between strain and the displacement field, u_i, is given by

$$\varepsilon_{ij} = \frac{1}{2}\left(\frac{\partial u_i}{\partial x_j} + \frac{\partial u_j}{\partial x_i}\right), \tag{7}$$

where the nomenclature is as previously defined.

2.2. Boundary conditions

For a unique solution to the governing equations, appropriate boundary conditions are to be prescribed. The boundary of the solid domain is split into two parts: $\partial\mathcal{V}_u$ where the displacement u_i^p is prescribed and $\partial\mathcal{V}_t$ where the surface traction τ_i^p is prescribed:

$$u_i = u_i^p \qquad \text{on} \qquad \partial\mathcal{V}_u \tag{8}$$

$$\sigma_{ij} n_j = \tau_i^p \qquad \text{on} \qquad \partial\mathcal{V}_t \tag{9}$$

where n_j is the outward pointing unit normal vector.

3. Spatial Discretisation

For the purpose of this work we use a vertex-centred edge-based finite volume method. In this method, control volumes are constructed by joining edge centres and element centres to form a dual mesh and the unknown

variables are stored at nodes or vertices of the original mesh. This approach utilises edge-based data-structures and is preferred for this work due to its increased efficiency compared to element-based approaches [19, 20].

Consider the governing equation, Equation (1). Assuming the body forces, f_i, to be negligible, expressing the acceleration, a_i, as the rate of change of velocity, v_i, casting the equation into integral or weak form by integrating over an arbitrary spatial subdomain, $\mathcal{V}_m$, and applying the divergence theorem of Gauss gives

$$\rho \frac{d}{dt} \int_{\mathcal{V}_m} v_i d\mathcal{V} = \oint_{\mathcal{A}_m} \sigma_{ij} \cdot n_j d\mathcal{A}, \tag{10}$$

where $\mathcal{A}_m$ is the surface enclosing $\mathcal{V}_m$ and $n_j = (n_1, n_2)$ is the outward pointing unit-vector normal to $\mathcal{A}$.

In the standard edge-based vertex-centred finite volume method, the dependent variables are stored at nodes around which control volumes are constructed. In 2D, these control volumes are constructed by joining the midpoints of edges with element centroids and in such a way that only one node lies within each control volume. The set of surfaces forming the control volumes are referred to as a dual-mesh. This is shown schematically for a node m in Figure 1 [17]. In the figure, $\mathcal{V}_m$ is the control volume associated with node m. Its bounding surface $\mathcal{A}_m$ is composed of a number of surfaces which are defined based on their associated edges. For example, $\mathcal{A}_{mn}$ is the surface segment intersecting the edge Υ_{mn} which connects nodes m and n.

The surface integrals in Equation (10) are now calculated in an edge-wise manner, i.e. the surface integral is expressed as the sum over all the edges connecting the control volume:

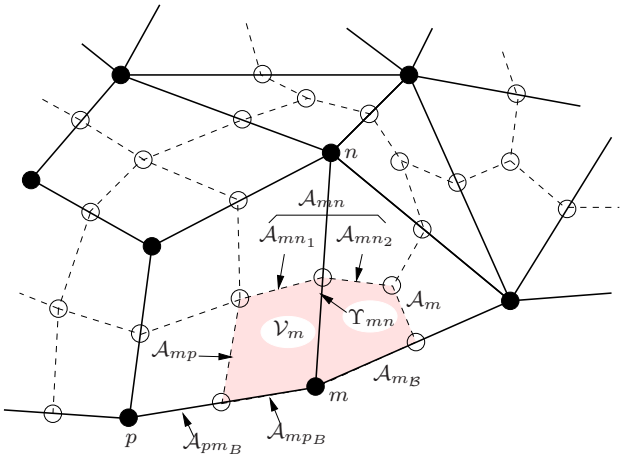

Figure 1: Schematic of the construction of a dual-mesh

$$\rho \frac{d}{dt} \int_{\mathcal{V}_m} v_i d\mathcal{V} = \sum_{\Upsilon_{mn} \cap \mathcal{V}_m} \sigma_{ij} \cdot C_{j:mn} + \sum_{\Upsilon^B_{mn} \cap \mathcal{V}_m} \sigma_{ij} \cdot B_{j:mn} \tag{11}$$

where C_{mn} is the edge-coefficient for an internal edge Υ_{mn} and B_{mn} the edge-coefficient for edges that lie on the boundary of the domain, denoted by $\mathcal{A}_{m_\mathcal{B}}$ in Figure 1. An internal edge-coefficient is defined as the area of the bounding surface of a particular edge in a control volume multiplied by the outward pointing unit-vector normal to its face; therefore

$$C_{j:mn} = \sum_{\mathcal{A}_{mn_t} \in \mathcal{A}_{mn}} n_{j:mn_t} \mathcal{A}_{mn_t}, \tag{12}$$

where $\mathcal{A}_{mn_t}$ is a segment of the surface $\mathcal{A}_{mn}$ and $n_{j:mn_t}$ is the unit-vector normal to $\mathcal{A}_{mn_t}$. For the edge Υ_{mn} shown in Figure 1, the edge-coefficient is comprised of two surfaces $t = 1$ and $t = 2$.

Boundary edge-coefficients are computed in a similar way to their internal edge counterparts:

$$B_{j:mn} = \sum_{\mathcal{A}_{mn_{\mathcal{B}^t}} \in \mathcal{A}_{mn_{\mathcal{B}}}} n_{j:mn_{\mathcal{B}^t}} \mathcal{A}_{mn_{\mathcal{B}^t}} \tag{13}$$

where $n_{j:mn_{\mathcal{B}^q}}$ is the outward pointing unit-vector normal to the boundary surface segment $\mathcal{A}_{mn_{\mathcal{B}^q}}$. For the case shown in Figure 1, Υ_{mp} is a boundary edge and $\mathcal{A}_{mp_{\mathcal{B}}}$ is the domain boundary surface associated with this edge. Therefore, for a 2D domain as above, t is always equal to 1 in Equation (13).

If following the standard edge-based finite volume method [17], the displacement gradients are evaluated numerically at the nodes or vertices. Therefore, referring to Figure 1 and following from Gauss's divergence theorem, the displacement gradients for node m are given by:

$$\left.\frac{\partial u_i}{\partial x_j}\right|_m = \frac{1}{\mathcal{V}_m} \oint_{\mathcal{A}_m} u_i \cdot n_j d\mathcal{A}_m = \frac{1}{\mathcal{V}_m} \sum_{\Upsilon_{mn} \cap \mathcal{V}_m} u_{i:mn} \cdot C_{j:mn} \tag{14}$$

where $u_{i:mn}$ is the linearly-interpolated displacement at the face:

$$u_{i:mn} \approx \frac{1}{2}(u_{i:m} + u_{i:n}). \tag{15}$$

In the edge-based procedure, the stresses are calculated at the faces of the dual-cells using a compact stencil [21, 22]. The displacement gradients at the faces are therefore given by:

$$\left.\frac{\partial u_i}{\partial x_j}\right|_{mn} \approx \frac{u_{i:n} - u_{i:m}}{|\bar{l}|}\frac{l_j}{|\bar{l}|} + \frac{1}{2}\left(\left.\frac{\partial u_i}{\partial x_j}\right|_m + \left.\frac{\partial u_i}{\partial x_j}\right|_n\right)\Bigg|_{normal} \tag{16}$$

where $\bar{l}$ is the edge-length, l_j is the j component of the vector from node m to n and $|_{normal}$ indicates the component in the direction normal to the edge.

The strains evaluated using Equation (7) and these displacement gradients are referred to as node-based strains. Finally, the stresses, required to evaluate the integrals in Equation (11), are computed using Equation (2).

3.1. Proposed hybrid finite volume method

As is clear from the above, with the standard vertex-centred method, strains (displacement gradients) are evaluated at the nodes or vertices. As will be shown in this paper, this results in unwanted inaccuracies when modelling beams under bending. An alternative would be to evaluate strains at element centres, similar to the finite element method, as proposed in [23]. In this case, displacement gradients for element M in Figure 2 are calculated as:

$$\left.\frac{\partial u_i}{\partial x_j}\right|_M = \frac{1}{\mathcal{V}_M} \sum_{\Upsilon_M \cap \mathcal{V}_M} \left(u_{i:MN} \cdot n_{j:MN} \mathcal{A}_{MN} \right) \tag{17}$$

where $\mathcal{A}_{MN}$ is the surface segment between elements M and N and $u_{i:MN}$ is the linearly-interpolated displacement of this surface (note that in 2D $u_{i:mn}$ and $u_{i:MN}$ are identical):

$$u_{i:MN} \approx \frac{1}{2}(u_{i:m} + u_{i:n}). \tag{18}$$

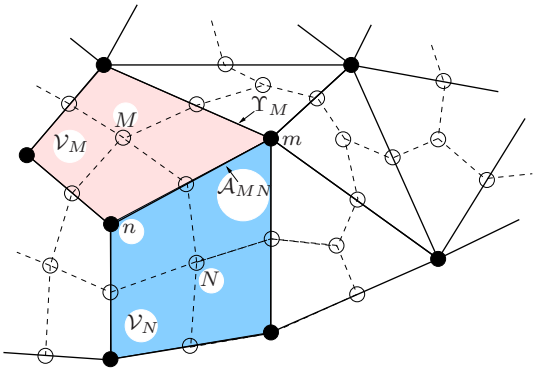

Figure 2: Schematic of a mesh showing the calculation of element-based gradients

The displacement gradients at the faces are obtained by averaging their values between the two connecting elements:

$$\left.\frac{\partial u_i}{\partial x_j}\right|_{mn} \approx \frac{1}{2}\left(\left.\frac{\partial u_i}{\partial x_j}\right|_{M} + \left.\frac{\partial u_i}{\partial x_j}\right|_{N}\right). \tag{19}$$

The strains evaluated using these displacement gradients are referred to as element-based strains.

On evaluation of the element-based strain finite volume method, it was found to suffer from odd-even decoupling on structured meshes. This is because displacements appear only in the combination $(u_{i:m} + u_{i:n})$. An improved hybrid finite volume method to remedy the odd-even decoupling is therefore proposed. This method uses element-based strains for the shear components, but node-based strains for the normal components. Therefore, Equation (19) is used for the displacement gradients in ε_{ij} with $i \neq j$ and Equation (16) in ε_{ij} with $i = j$. Note that this is similar to the selective integration approach [16] used in the finite element method to eliminate spurious modes, where different Gauss quadrature integration rules are used for the shear and normal strain contributions to the stiffness matrix.

4. Solution Procedure

In this work, a matrix-free approach is employed for solving the governing equations. This is more common in computational fluid dynamics, but is equally applicable to structural mechanics and the procedure is described below.

The temporal term in Equation (11) is discretised using a dual-timestepping solution procedure [24, 25], such that second-order temporal accuracy is achieved and the equations are solved in a matrix-free iterative process.

This dual-timestepping procedure is independent of the spatial discretisation strategy employed, viz. finite volume or finite element. For the finite volume method in this work, Equation (11), the spatial terms are grouped together and the equation re-written as follows:

$$\rho \mathcal{V}_m \frac{dv_i}{dt} = RHS_i \tag{20}$$

where RHS denotes the discretised spatial terms, the subscript m indicates the node number and i the component in the x_1- or x_2-direction.

Now, a pseudo-time temporal term is added to the left-hand-side of the equation and the real-time temporal term added as a source term to the right-hand-side of the equation. Equation (20) becomes

$$\rho \frac{dv_i}{d\tau} \mathcal{V}_m = RHS_i - \rho \frac{dv_i}{dt} \mathcal{V}_m. \tag{21}$$

Equation (21) is solved explicitly until pseudo-steady state is reached, i.e. $\frac{dv_i}{d\tau} = 0$. This makes Equations (20) and (21) equivalent and means that the actual governing equations are solved implicitly but without the need for matrix inversion.

Since the accuracy of the pseudo-time temporal term is of little consequence, as it becomes zero upon convergence, it is discretised to first-order accuracy while the real-time temporal term is discretised to second-order accuracy, giving

$$\rho \frac{v_i^{\tau+\Delta\tau} - v_i^{\tau}}{\Delta\tau} \mathcal{V}_m \approx RHS_i - \rho \frac{3v_i^{\tau+\Delta\tau} - 4v_i^{n} + v_i^{n-1}}{2\Delta t} \mathcal{V}_m \tag{22}$$

where Δt is the real-timestep size and $\Delta\tau$ the pseudo-timestep size.

To introduce the primary variable, displacement, into the equation, we

simply note that velocity is the temporal rate of change of displacement, u_i,

$$\frac{du_i}{dt} = v_i. \tag{23}$$

Discretising the displacement equation using the same approach as for velocity above, gives

$$\frac{u_i^{\tau+\Delta\tau} - u_i^{\tau}}{\Delta\tau} \approx v_i^{\tau+\Delta\tau} - \frac{3u_i^{\tau+\Delta\tau} - 4u_i^{n} + u_i^{n-1}}{2\Delta t}. \tag{24}$$

The solution procedure involves solving for velocity v_i and displacement u_i in an iterative fashion. In order to ensure stability for all cases, a second-order accurate single-step procedure [26] is employed as follows:

1. At timestep $n+1$, loop over all nodes i and set $u_i^{\tau} = u_i^{n}$ and $v_i^{\tau} = v_i^{n}$.
2. Calculate a projected displacement by discretising Equation (23) as follows:
$$\overline{u}_i^{\tau} = u_i^{\tau} + \Delta\tau\left(v_i^{\tau} - \frac{3u_i^{\tau} - 4u_i^{n} + u_i^{n-1}}{2\Delta t}\right). \tag{25}$$
3. Using $\overline{u}_i^{\tau}$, compute the strain field using Equation (7) and the stress field using Equation (2).
4. Solve for $v_i^{\tau+\Delta\tau}$ explicitly using the discretised form of the equilibrium equations, Equation (22).
5. Update the displacement at $\tau+\Delta\tau$ using the latest velocity $v_i^{\tau+\Delta\tau}$ and the acceleration, calculated in step 3, i.e.
$$u_i^{\tau+\Delta\tau} = u_i^{\tau} + \Delta\tau\left(v_i^{\tau+\Delta\tau} - \frac{3u_i^{\tau+\Delta\tau} - 4u_i^{n} + u_i^{n-1}}{2\Delta t}\right) + \frac{1}{2}\Delta\tau^2\frac{1}{\rho\mathcal{V}_m}\left(RHS_i|_{\overline{u}_i^{\tau}} - \rho\frac{3v_i^{\tau+\Delta\tau} - 4v_i^{n} + v_i^{n-1}}{2\Delta t}\mathcal{V}_m\right). \tag{26}$$
6. The residuals of the equilibrium equation are calculated, $\mathrm{Res}_i = (v_i^{\tau+\Delta\tau} - v_i^{\tau})/\Delta\tau$.

7. The overall residual is calculated from the root mean square of that at each node, therefore $\text{Res} = \sqrt{\sum_i^n (\text{Res}_i)^2/n}$, where n is the number of nodes.
8. If the residuals are greater than the convergence tolerance, Steps 2 to 5 are repeated.
9. If the residuals are less than the convergence tolerance, $v_i^{\tau+\Delta\tau} \approx v_i^{\tau}$, and the real-timestep is terminated. Therefore, $v_i^{n+1} = v_i^{\tau+\Delta\tau}$ and $u_i^{n+1} = u_i^{\tau+\Delta\tau}$. The next timestep is entered by proceeding to Step 1.

The dual-timestepping procedure, described above is explicit in pseudo-time, which means it is a conditionally stable scheme and a limit exists on the pseudo-timestep size $\Delta\tau$. The procedure is implicit in real-time, thus the scheme is stable for any choice of the real-timestep size Δt.

A stable solution process exists if $\Delta\tau < \Delta\tau_{\text{cr}}$, where $\Delta\tau_{\text{cr}}$ is the critical timestep size [26] defined by the following expression:

$$\frac{\Delta x_i}{\Delta\tau_{\text{cr}}} = \sqrt{\frac{K}{\rho_o}} + \sqrt{\frac{G}{\rho_o}} \tag{27}$$

where Δx_i is the effective mesh spacing in the i-direction and K and G are the bulk and shear modulus,

$$K = \frac{E}{3(1-2\nu)}, \tag{28}$$

$$G = \frac{E}{2(1+\nu)}. \tag{29}$$

5. Results and Discussions

The accuracy of the proposed finite volume method is evaluated via application to 2D test problems with increasing degree of complexity. The results are compared against linear and higher-order finite element formulations.

5.1. Uniaxial tension

The first test problem considered was that of a 2D body in uniaxial tension, as shown in Figure 3. The solid has a Young's modulus of $E = 210$ GPa, Poisson's ratio $\nu = 0.3$ and a length and width of 1 mm. Plane strain was assumed in the analysis. The mesh consisted of a single cell.

The normal stress, σ_{11}, is plotted against tip displacement, c, in Figure 4. The finite volume and finite element formulations give exactly the same results; the σ_{11} stress increases linearly with an increase in c for small displacements.

5.2. Simple shear

A 2D body subjected to the deformation

$$x_1 = X_1 + cX_2 \tag{30}$$

$$x_2 = X_2, \tag{31}$$

which results in the body undergoing simple shear as shown in Figure 5, was considered next. The same geometry, mesh and material properties as the previous case, were used.

Figure 3: Solid body in uniaxial tension

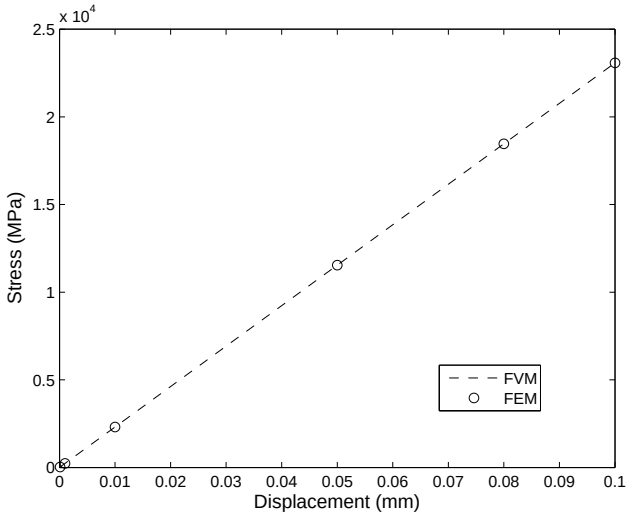

Figure 4: Comparison of σ_{11} stress for uniaxial tension

Both the σ_{11} and σ_{12} stress components are plotted against tip displacement, c, in Figure 6. Again, all the finite volume and finite element formulations give the correct results; the linear elasticity formulation predicts zero

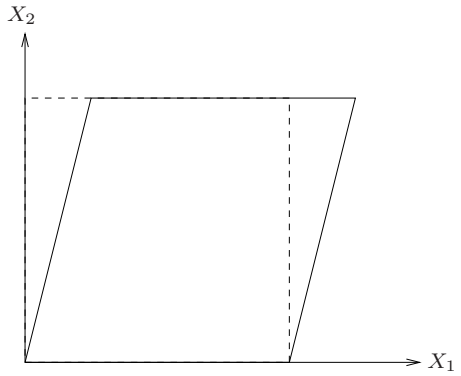

Figure 5: Solid body in simple shear

normal stress components and the shear stress, σ_{12}, increases linearly with an increase in c.

5.3. Pure bending

The next test-case considered was that of a thick beam in pure bending, Figure 7. The beam was clamped at one end and subjected to a moment at the free end. The material properties used were a Young's modulus $E = 210$ GPa and Poisson's ratio $\nu = 0$. The length $l = 6$ mm, height $h = 1$ mm and the plane stress assumption were used.

The analytical solution for the tip displacement of the beam can be derived from first principles [27] and is given by

$$u_1 = \frac{Mx_1x_2}{EI} \tag{32}$$

$$u_2 = -\frac{Mx_1^2}{2EI}, \tag{33}$$

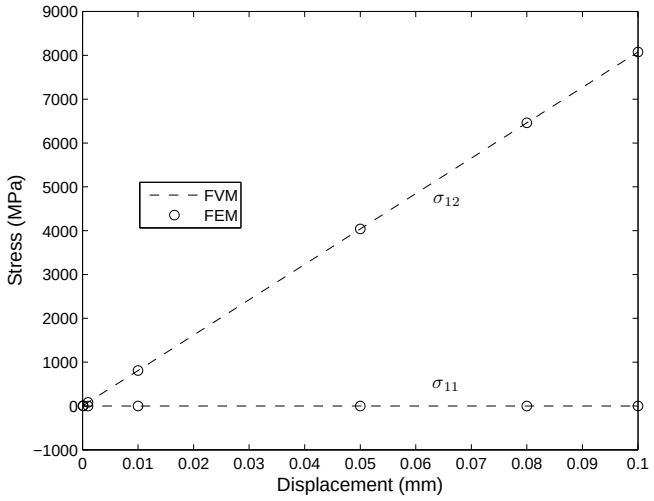

Figure 6: Comparison of σ_{11} and σ_{12} stress for simple shear

where M is the bending-moment at the free end and I is the moment of inertia of the cross-section of the beam. Due to the known sensitivity of linear methods to element aspect ratio, meshes with varying aspect ratios (Figure 8) were used to analyse this problem. The element aspect ratio is defined as the ratio of the element length to its height. Note that the number of elements in each mesh were chosen so that by keeping the total number of elements constant, varying aspect ratios could be obtained. The free end is treated as a surface traction boundary and the bending-moment, M, is introduced by applying consistent nodal loads at each node along this boundary such that global equilibrium is satisfied.

The resulting tip displacements when using the finite volume and linear four-node (Q4) finite element formulations are shown in Figure 9. For this type of problem, it is well documented that the Q4 finite element formulation suffers from shear locking [16], i.e. when subjected to pure bending, Q4 elements produce a shear strain contribution in addition to the expected bending strain. This parasitic shear strain absorbs strain energy and to compensate the displacements decrease or the structure stiffens or locks. This shear locking effect is magnified when the aspect ratio (ratio of the element

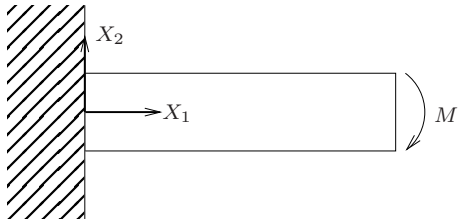

Figure 7: Cantilever beam in pure bending

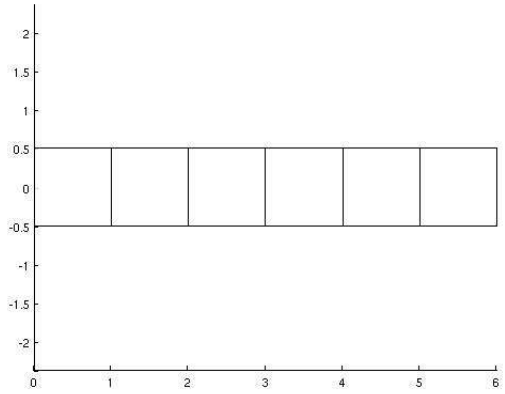

(a) Aspect ratio = 1

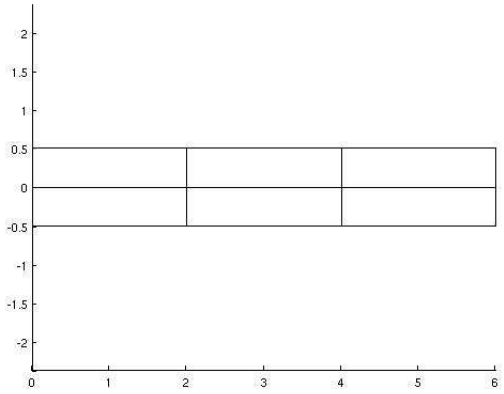

(b) Aspect ratio = 4

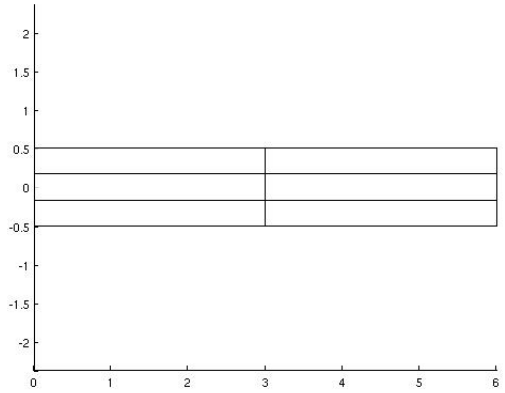

(c) Aspect ratio = 9

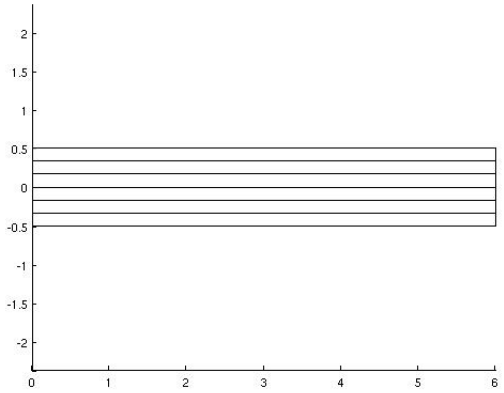

(d) Aspect ratio = 36

Figure 8: Meshes with varying element aspect ratios used for analysing a beam in pure bending

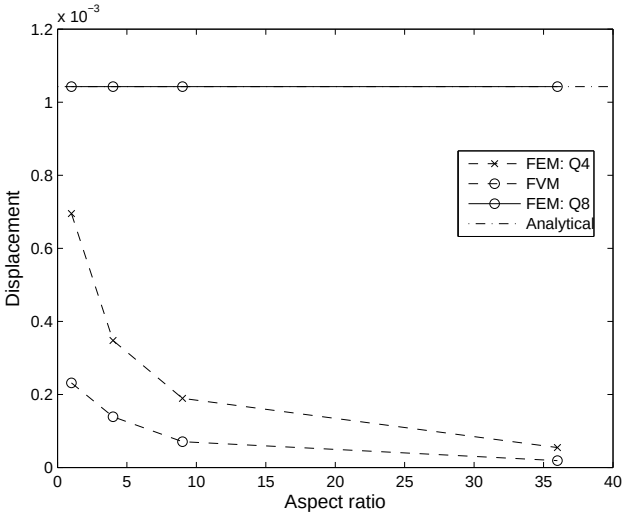

Figure 9: Tip displacement as a function of element aspect ratio for a beam in pure bending

length to its height) is increased, i.e. as the elements become long and thin, the structure becomes stiffer and results in decreasing displacements. This effect can clearly be seen in the figure. As shown in Figure 9, the standard finite volume method also suffers from this ailment. The higher-order eight-node (Q8) finite element formulation is locking-free and is able to predict the exact tip displacement for this problem, also shown in Figure 9.

However, using the proposed hybrid finite volume method it can be seen (Figure 10) that this formulation is completely locking-free, which is a remarkable quality for a linear method. It is therefore superior to both the standard vertex-centred finite volume method and the Q4 finite element method.

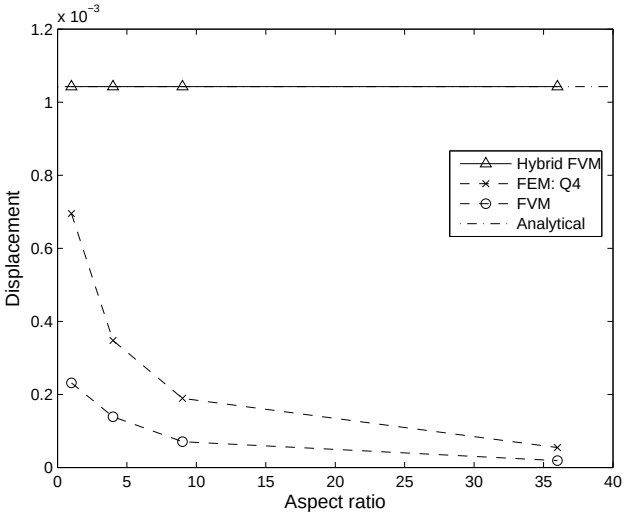

Figure 10: Tip displacement as a function of element aspect ratio using the hybrid finite volume method

5.4. Cantilever beam in bending

The final test-case analysed was that of a thin cantilever beam subjected to a tip load at the free end, as shown in Figure 11. The beam has a Young's modulus of 0.2 MPa and Poisson's ratio of zero. A combination of both bending and shear deformation effects are present in the beam. The analytical solution is given by [27]:

$$u_1 = \frac{P}{EI}\left(- Lx_1x_2 + c^2x_2 + \frac{1}{2}x_1^2x_2 - \frac{1}{3}x_2^3\right) \tag{34}$$

$$u_2 = \frac{P}{EI}\left(\frac{1}{2}Lx_1^2 - \frac{1}{6}x_1^3\right) \tag{35}$$

where P is the magnitude of the tip load, L is the length of the beam and $2c$ is the thickness of the beam.

A meshing strategy similar to the previous case was employed to investigate aspect ratio sensitivity. The calculated tip displacement resulting from both finite volume methods, as well as linear four-node (Q4) and higher-order eight-node (Q8) finite element methods are shown in Figure 12. The locking effect is again clearly evident with the standard vertex-centred finite volume and Q4 finite element formulations. In contrast, with the hybrid method, although the results are initially inaccurate for small element aspect ratios, the accuracy now improves with an increase in aspect ratio as expected, since the structure does not stiffen or lock. The Q8 finite element method offers exact accuracy in all cases.

For the purpose of the numerical investigation, a constant element aspect ratio of 20/3 was used and meshes of increasing refinedness generated by successively doubling the number of cells in both directions. A plot of the logarithm of the error of tip displacements vs. the logarithm of the mesh size is shown in Figure 13. The negative of the gradient of this curve gives the rate of convergence: 2.0 for the hybrid formulation and 1.9 for the vertex-

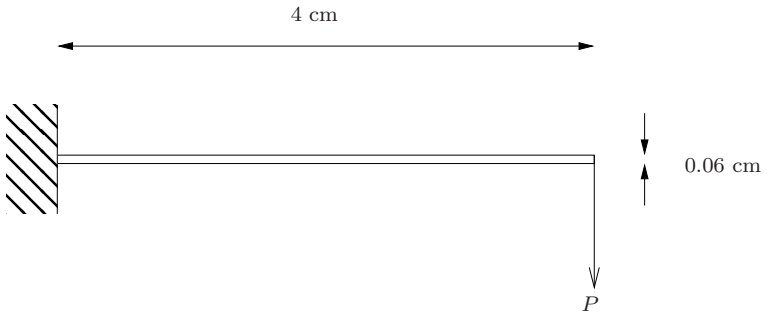

Figure 11: Thin cantilever beam subjected to a concentrated tip load

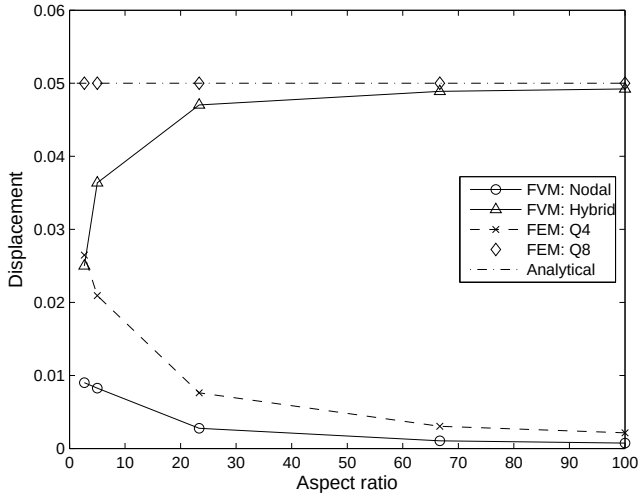

Figure 12: Tip displacement as a function of element aspect ratio for a thin cantilever beam subjected to a concentrated tip load

formulation. Though both finite volume methods tend to second-order accuracy, the hybrid formulation achieves this on a considerably coarser mesh while resulting in significantly smaller errors. To develop a more fundamental understanding of this, the next section details a formal error analysis of the two methods.

6. Error Analysis: Beams Subjected to Bending

To understand the difference in accuracy between the vertex-centred and hybrid finite volume formulations, a detailed analytical error analysis and comparison were conducted on both formulations and the results evaluated on modelling beams under bending.

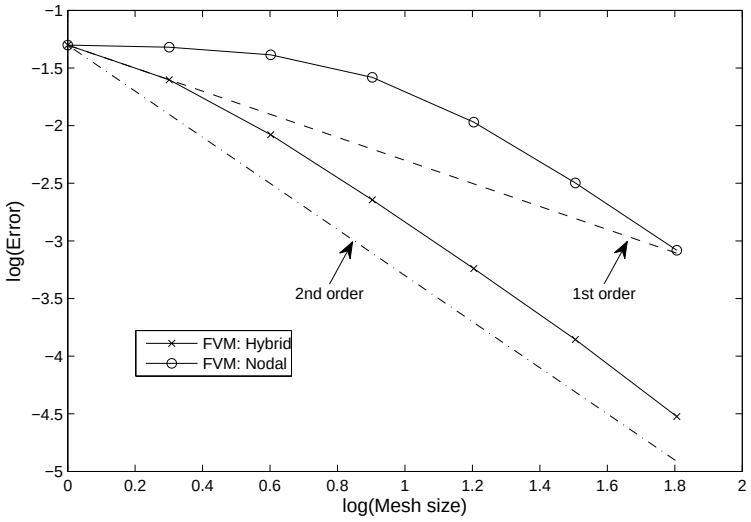

Figure 13: Convergence rate of displacements

6.1. Analytical analysis

Consider again the governing equation, Equation (1). Since we are only interested in the spatial accuracy, we neglect the temporal term and consider only the steady-state problem, i.e. $a_i = 0$. The equation simplifies to:

$$\frac{\partial \sigma_{ij}}{\partial x_j} = 0. \tag{36}$$

Numerical error is introduced by the discretisation, which can be expressed by:

$$\frac{\partial \sigma_{ij}}{\partial x_j} = \frac{1}{\mathcal{V}_m}\left(\sum_{\Upsilon_{mn} \cap \mathcal{V}_m} \sigma_{ij} \cdot C_{j:mn} + \sum_{\Upsilon^B_{mn} \cap \mathcal{V}_m} \sigma_{ij} \cdot B_{j:mn} \right) + \mathrm{Error}_{i:m}. \tag{37}$$

The exact form of this $\mathrm{Error}_{i:m}$ term may be determined analytically. For a Poisson's ratio of zero, which was used for the problems in the previous

section, the stress-strain relationship, Equation (2), simplifies to:

$$\sigma_{ij} = E\varepsilon_{ij}. \tag{38}$$

The strain-displacement relationship for the small displacement case is:

$$\varepsilon_{ij} = \frac{1}{2}\left(\frac{\partial u_i}{\partial x_j} + \frac{\partial u_j}{\partial x_i}\right). \tag{39}$$

Substituting Equation (38) and Equation (39) into Equation (37) gives an equation expressed in terms of displacements, from which the numerical errors can be determined.

In this work only structured equi-spaced meshes are considered for the solid, which further simplifies the analysis. Consider first the vertex-centred formulation for the case of an internal (non boundary) node (Figure 14(a)).

Substituting the expressions for the displacement gradients, Equation (16), and expanding each term using Taylor series expansions about the node, the

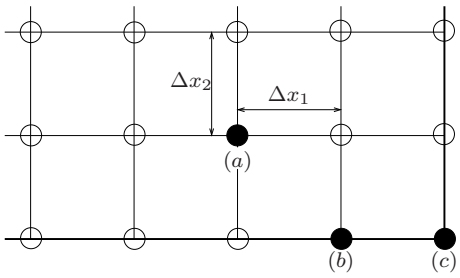

Figure 14: Schematic of the mesh indicating an internal, boundary and corner node

discrete expression for the leading error-term is given by:

$$\text{Error}_i = -\frac{E}{2}\left(\frac{1}{6}\frac{\partial^4 u_i}{\partial x_i^4}\Delta x_i^2 + \frac{1}{12}\frac{\partial^4 u_i}{\partial x_k^4}\Delta x_k^2 + \frac{1}{6}\frac{\partial^4 u_k}{\partial x_i^3 \partial x_k}\Delta x_i^2 + \frac{1}{6}\frac{\partial^4 u_k}{\partial x_i \partial x_k^3}\Delta x_k^2\right) \quad (40)$$

with

$$i = 1; k = 2 \qquad \text{for the } x_1\text{-momentum equation}$$

$$i = 2; k = 1 \qquad \text{for the } x_2\text{-momentum equation.}$$

Similarly, for a boundary node (Figure 14(b)) the leading-order error terms for the tangential and normal components of the momentum equations respectively, are:

$$\text{Error}_t = -\frac{E}{2}\left(\frac{1}{3}\frac{\partial^3 u_t}{\partial x_n^3}\Delta x_n + (-1)^p\frac{1}{2}\frac{\partial^3 u_n}{\partial x_t \partial x_n^2}\Delta x_n + (-1)^p\frac{1}{3}\frac{\partial^3 u_n}{\partial x_t^3}\frac{\Delta x_t^2}{\Delta x_n} + \frac{1}{6}\frac{\partial^4 u_t}{\partial x_t^4}\Delta x_t^2\right) \quad (41)$$

$$\text{Error}_n = -\frac{E}{2}\left((-1)^p\frac{1}{2}\frac{\partial^3 u_t}{\partial x_t \partial x_n^2}\Delta x_n\right) \quad (42)$$

where subscripts n and t denote coordinates normal and tangential to the boundary respectively, $p = 1$ for the top and right boundaries and $p = 2$ for the bottom and left boundaries.

Finally, for a corner node (Figure 14(c)) the leading-order error term is:

$$\text{Error}_i = -\frac{E}{2}\left((-1)^p\frac{\partial^2 u_k}{\partial x_i^2}\frac{\Delta x_i}{\Delta x_k}\right) \quad (43)$$

with

$$i = 1; k = 2 \qquad \text{for the } x_1\text{-momentum equation}$$

$$i = 2; k = 1 \qquad \text{for the } x_2\text{-momentum equation}$$

$$p = 1 \qquad \text{for the top-left and bottom-right corners}$$

$$p = 2 \qquad \text{for the top-right and bottom-left corners.}$$

Two important conclusions can be derived from the leading-order error terms for the standard vertex-centred formulation above. Firstly, the truncation error is of order $O(\Delta x_i^2)+O(\Delta x_k^2)$ at internal nodes, $O(\Delta x_n)+O(\frac{\Delta x_t^2}{\Delta x_n})$ at boundary nodes and $O(\frac{\Delta x_i}{\Delta x_k})$ at corner nodes. Therefore, second-order rate of convergence is expected for internal nodes but only first-order for boundary nodes and zero-order for corner nodes. This correlates with the results in Figure 13: the number of boundary and corner nodes compared to internal nodes decreases as the mesh gets finer and the scheme tends towards a second-order rate of convergence. In addition, since the coefficients of the leading-order error terms at internal nodes are fourth-order derivatives, the formulation will be exact at internal nodes for a displacement field described by a cubic polynomial. However, at boundary nodes the formulation can only represent quadratic fields exactly and similarly only linear fields at corner nodes.

Using the same approach for the hybrid formulation, but substituting Equation (19) for the displacement gradients in ε_{ij} with $i \neq j$ and Equation (16) in ε_{ij} with $i = j$, the leading-order error term at the internal node (Figure 14(a)) is:

$$\text{Error}_i = -\frac{E}{2}\left(\frac{1}{6}\frac{\partial^4 u_i}{\partial x_i^4}\Delta x_i^2 + \frac{1}{12}\frac{\partial^4 u_i}{\partial x_k^4}\Delta x_k^2 + \frac{1}{6}\frac{\partial^4 u_k}{\partial x_i^3 \partial x_k}\Delta x_i^2 + \right.$$
$$\left. \frac{1}{6}\frac{\partial^4 u_k}{\partial x_i \partial x_k^3}\Delta x_k^2 + \frac{1}{4}\frac{\partial^4 u_i}{\partial x_i^2 \partial x_k^2}\Delta x_i^2\right) \quad (44)$$

where the nomenclature is as previously defined.

For a boundary node (Figure 14(b)):

$$\text{Error}_t = -\frac{E}{2}\left(\frac{1}{3}\frac{\partial^3 u_t}{\partial x_n^3}\Delta x_n + (-1)^p\frac{1}{2}\frac{\partial^3 u_n}{\partial x_t \partial x_n^2}\Delta x_n + (-1)^p\frac{1}{3}\frac{\partial^3 u_n}{\partial x_t^3}\frac{\Delta x_t^2}{\Delta x_n} + (-1)^q\frac{\partial^3 u_t}{\partial x_t^2 \partial x_n}\frac{\Delta x_t^2}{\Delta x_n} + \frac{1}{6}\frac{\partial^4 u_t}{\partial x_t^4}\Delta x_t^2\right) \quad (45)$$

$$\text{Error}_n = -\frac{E}{2}\left((-1)^p\frac{1}{2}\frac{\partial^3 u_t}{\partial x_t \partial x_n^2}\Delta x_n + (-1)^q\frac{1}{2}\frac{\partial^3 u_n}{\partial x_t^2 \partial x_n}\Delta x_n\right) \quad (46)$$

where $q = 1$ for the left and right boundaries and $q = 2$ for the bottom and left boundaries and the rest of the symbols are as previously defined.

Finally, for a corner node (Figure 14(c)) the leading-order error term is:

$$\text{Error}_i = -\frac{E}{2}\left((-1)^p\frac{\partial^2 u_k}{\partial x_i^2}\frac{\Delta x_i}{\Delta x_k} - \frac{\partial^2 u_i}{\partial x_i \partial x_k}\frac{\Delta x_i}{\Delta x_k}\right). \quad (47)$$

Again these results correlate with those obtained from the numerical analysis (Figure 13): as the meshes get finer, the number of internal nodes is significantly more than boundary and corner nodes and both schemes tend towards second-order accuracy. The truncation errors of the hybrid formulation are compared with that of the vertex-centred formulation in Table 1. As can be seen in the table, the truncation errors are of the same order for both formulations. Furthermore, based on the coefficients of the leading-order error terms, the hybrid formulation indicates the same order of accuracy as that of the vertex-centred formulation. However, the hybrid formulation is composed of error terms that oppose each other, which may explain the greater accuracy. These will be analysed on specific test-cases next.

6.2. Application to beam in bending

For the pure bending test-case considered in the previous section, the analytical solution for the tip displacement of the beam is given by Equations (32) and (33). Since it is a quadratic displacement field, the hybrid

	Vertex-centred FVM		Hybrid FVM	
Internal node	$O(\Delta x_i^2)$ / $O(\Delta x_k^2)$	2nd-order	$O(\Delta x_i^2)$ / $O(\Delta x_k^2)$	2nd-order
Boundary node	$O(\Delta x_t)$ / $O(\frac{\Delta x_n^2}{\Delta x_t})$	1st-order	$O(\Delta x_t)$ / $O(\frac{\Delta x_n^2}{\Delta x_t})$	1st-order
Corner node	$O(\frac{\Delta x_i}{\Delta x_k})$	zero-order	$O(\frac{\Delta x_i}{\Delta x_k})$	zero-order

Table 1: Order of accuracy of the vertex-centred and hybrid formulations

	Vertex-centred FVM	Hybrid FVM
Internal node	0	0
Boundary node	0	0
Corner node	$\frac{M}{2I}\frac{\Delta x_1}{\Delta x_2}$	0

Table 2: Errors of vertex-centred and hybrid formulations for a beam in pure bending

FVM's superiority over the Q4 FEM and vertex-centred FVM is an interesting finding. As shown above, both the hybrid and vertex-centred formulations should contain error terms at the corners. To understand this difference in accuracy, the exact errors are obtained by substituting the analytical solution into the expressions for the errors above. These are summarised in Table 2.

The error expressions in Table 2 confirm the numerical results obtained for the beam in pure bending test-case (Figure 10). The errors for the hybrid formulation cancel out at the corner nodes and the exact solution is obtained. However, with the vertex-centred formulation the error remains. Furthermore, this error scales as $\frac{\Delta x_1}{\Delta x_2}$, i.e. the error increases with an increase

	Vertex-centred FVM	Hybrid FVM
Internal node	0	0
Boundary node (top/bottom):		
x_1-momentum	$(-1)^{p+1}\left(\frac{1}{3}\frac{P}{I}\Delta x_2 + \frac{1}{6}\frac{P}{I}\frac{\Delta x_1^2}{\Delta x_2}\right)$	$(-1)^{p+1}\left(\frac{1}{3}\frac{P}{I}\Delta x_2 + \frac{1}{6}\frac{P}{I}\frac{\Delta x_1^2}{\Delta x_2}\right) + (-1)^{p}\frac{1}{4}\frac{P}{I}\frac{\Delta x_1^2}{\Delta x_2}$
x_2-momentum	0	0
Boundary node (right):		
x_1-momentum	0	0
x_2-momentum	$-\frac{1}{12}\frac{P}{I}\Delta x_1 + \frac{1}{3}\frac{P}{I}\frac{\Delta x_2^2}{\Delta x_1}$	$-\frac{1}{12}\frac{P}{I}\Delta x_1 + \frac{1}{3}\frac{P}{I}\frac{\Delta x_2^2}{\Delta x_1}$
Corner node (right):		
x_1-momentum	0	0
x_2-momentum	$(-1)^{p}\frac{Pc}{I}\frac{\Delta x_2}{\Delta x_1}$	$(-1)^{p}\frac{Pc}{I}\frac{\Delta x_2}{\Delta x_1}$
Corner node (left):		
x_1-momentum	$(-1)^{p}\frac{PL}{2I}\frac{\Delta x_1}{\Delta x_2}$	0
x_2-momentum	$(-1)^{p}\frac{Pc}{I}\frac{\Delta x_2}{\Delta x_1}$	$(-1)^{p}\frac{Pc}{I}\frac{\Delta x_2}{\Delta x_1}$

Table 3: Errors of vertex-centred and hybrid formulations for a cantilever beam subjected to a tip load

in aspect ratio. This explains the shear locking effect observed above.

A similar approach can be followed to determine the exact errors of the two formulations for the cantilever beam subjected to a concentrated tip load (Figure 11). Substituting the analytical equations (Equations (34) and (35)) into the error expressions yields the leading-order error terms as shown in Table 3, with the nomenclature as previously defined.

The results in Table 3 show that for this test-case, the difference between the two formulations is in the x_1-momentum equation at the left corners of the beam. The vertex-centred formulation contains an error term that again

scales as $\frac{\Delta x_1}{\Delta x_2}$. This, again, explains the sensitivity to aspect ratio or shear locking effect present with the formulation. The corresponding error term for the hybrid formulation is zero. These analytical expressions correspond with the numerical results as shown in Figure 12; the hybrid finite volume method is not sensitive to large element aspect ratios, which results in more accurate solutions.

7. Conclusions

An edge-based vertex-centred finite volume method to model linear elastic structures was investigated and compared with the traditional finite element method in this work. Both formulations predict the analytical result for a simple tensile and simple shear test-case. When applied to a beam in bending, the finite volume formulation exhibits the undesirable characteristic of shear locking or sensitivity to element aspect ratio, similar to the Q4 finite element formulation. The structure becomes stiffer as the aspect ratio is increased.

To circumvent the locking deficiency, an enhanced hybrid finite volume formulation which uses both node- and element-based strains was proposed. It was shown to not stiffen or lock when the element aspect ratio increases, which is viewed as a significant improvement. A rigorous error analysis was presented, showing that both the vertex-centred and hybrid formulations have rates of convergence that tend towards 2, but the shear locking mechanism is overcome by the hybrid approach, which results in a considerably more accurate formulation.

References

[1] O. C. Zienkiewicz, R. L. Taylor, The Finite Element Method: Volume 2 - Solid Mechanics, 5th Edition, Butterworth-Heinemann, Oxford, 2000.

[2] S. V. Patankar, Numerical Heat Transfer and Fluid Flow, McGraw-Hill, New York, 1980.

[3] E. Oñate, M. Cervera, O. C. Zienkiewicz, A finite-volume format for structural mechanics, International Journal for Numerical Methods in Engineering 37 (1994) 181–201.

[4] M. A. Wheel, A finite-volume approach to the stress analysis of pressurized axisymmetric structures, International Journal of Pressure Vessels and Piping 68 (1996) 311–317.

[5] J. Fainberg, H.-J. Leister, Finite volume multigrid solver for thermoelastic stress analysis in anisotropic materials, Computer Methods in Applied Mechanics and Engineering 137 (1996) 167–174.

[6] M. A. Wheel, A finite volume method for analysing the bending deformation of thick and thin plates, Computer Methods in Applied Mechanics and Engineering 147 (1997) 199–208.

[7] A. K. Slone, C. Bailey, M. Cross, Dynamic solid mechanics using finite volume methods, Applied Mathematical Modelling 27 (2003) 69–87.

[8] N. Fallah, A cell vertex and cell centred finite volume method for plate bending analysis, Computer Methods in Applied Mechanics and Engineering 193 (2004) 3457–3470.

[9] I. Bijelonja, I. Demirdzic, S. Muzaferija, A finite volume method for incompressible linear elasticity, Computer Methods in Applied Mechanics and Engineering 195 (2006) 6378–6390.

[10] W. Pan, M. A. Wheel, Y. Qin, Six-node triangle finite volume method for solids with a rotational degree of freedom for incompressible material, Computers and Structures 88 (2010) 1506–1511.

[11] G. A. Taylor, C. Bailey, M. Cross, Solution of the elastic/visco-plastic constitutive equations: A finite volume approach, Applied Mathematical Modelling 19 (1995) 746–760.

[12] G. A. Taylor, C. Bailey, M. Cross, A vertex-based finite volume method applied to non-linear material problems in computational solid mechanics, International Journal for Numerical Methods in Engineering 56 (2003) 507–529.

[13] P. Wenke, M. A. Wheel, A finite volume method for solid mechanics incorporating rotational degrees of freedom, Computers and Structures 81 (2003) 321–329.

[14] N. Fallah, C. Bailey, M. Cross, G. A. Taylor, Comparison of finite element and finite volume methods application in geometrically nonlinear stress analysis, Applied Mathematical Modelling 24 (2000) 439–455.

[15] M. V. Jr., P. A. Munoz-Rojas, G. Filippini, On the accuracy of nodal stress computation in plane elasticity using finite volumes and finite elements, Computers and Structures 87 (2009) 1044–1057.

[16] R. D. Cook, D. S. Malkus, M. E. Plesha, R. J. Witt, Concepts and Applications of Finite Element Analysis, 4th Edition, John Wiley & Sons Ltd., United States, 2002.

[17] A. G. Malan, Investigation into the continuum thermodynamic modeling of investment casting shell-mould drying, Ph.D. thesis, University of Wales Swansea (2002).

[18] A. G. Malan, R. W. Lewis, An artificial compressibility CBS method for modelling heat transfer and fluid flow in heterogeneous porous materials, International Journal for Numerical Methods in Engineering 87 (2011) 412–423.

[19] R. Löhner, Applied CFD Techniques, John-Wiley and Sons Ltd., Chichester, 2001.

[20] Y. Zhao, B. Zhang, A high-order characteristics upwind FV method for incompressible flow and heat transfer simulation on unstructured grids, International Journal for Numerical Methods in Engineering 37 (1994) 3323–3341.

[21] P. I. Crumpton, P. Moinier, M. B. Giles, An unstructured algorithm for high Reynolds number flows on highly stretched meshes, in: C. Taylor, J. T. Cross (Eds.), Numerical Methods in Laminar and Turbulent Flow, Pineridge Press, 1997, pp. 561–572.

[22] A. G. Malan, R. W. Lewis, Modeling coupled heat and mass transfer in drying non-hygroscopic capillary particulate materials, Communications in Numerical Methods in Engineering 19 (9) (2003) 669–677.

[23] G. Xia, C.-L. Lin, An unstructured finite volume approach for structural dynamics in response to fluid motions, Computers and Structures 86 (2008) 684–701.

[24] A. Jameson, Time dependent calculations using multigrid, with applications to unsteady flows past airfoils and wings, AIAA Paper 91-1596.

[25] V. Venkatakrishnan, D. J. Mavriplis, Implicit method for the computation of unsteady flows on unstructured grids, Journal of Computational Physics 127 (1996) 380–397.

[26] O. C. Zienkiewicz, R. L. Taylor, The Finite Element Method: Volume 1 - The Basis, 5th Edition, Butterworth-Heinemann, Oxford, 2000.

[27] J. M. Gere, Mechanics of Materials, 6th Edition, Brooks/Cole-Thomson Learning, Belmont, 2004.